UC Irvine
UC Irvine Previously Published Works

Title
The Sensitivity of West African Convective Line Water Budgets to Land Cover

Permalink
https://escholarship.org/uc/item/3qr535q1

Journal
Journal of Hydrometeorology, 4(1)

ISSN
1525-755X

Authors
Mohr, Karen I
Baker, R David
Tao, Wei-Kuo
et al.

Publication Date
2003-02-01

DOI
10.1175/1525-7541(2003)004<0062:tsowac>2.0.co;2

Copyright Information
This work is made available under the terms of a Creative Commons Attribution License, availalbe at https://creativecommons.org/licenses/by/4.0/

Peer reviewed

eScholarship.org Powered by the California Digital Library
University of California

The Sensitivity of West African Convective Line Water Budgets to Land Cover

KAREN I. MOHR

Department of Earth and Atmospheric Sciences, University at Albany, State University of New York, Albany, New York

R. DAVID BAKER

Physics Department, Austin College, Sherman, Texas

WEI-KUO TAO

Laboratory for Atmospheres, NASA Goddard Space Flight Center, Greenbelt, Maryland

JAMES S. FAMIGLIETTI

Department of Earth System Science, University of California, Irvine, Irvine, California

(Manuscript received 28 August 2001, in final form 29 July 2002)

ABSTRACT

This study used a two-dimensional coupled land–atmosphere (cloud resolving) model to investigate the influence of land cover on the water budgets of convective lines in West Africa. Study simulations used the same initial sounding and one of three different land covers: a sparsely vegetated semidesert, a grassy savanna, and a dense evergreen broadleaf forest. All simulations began at midnight and ran for 24 h to capture a full diurnal cycle. During the morning, the forest had the highest latent heat flux, the shallowest, moistest, slowest growing boundary layer, and more convective available potential energy than the savanna and semidesert. Although the savanna and forest environments produced virtually the same total rainfall mass (semidesert 18%), the spatial and temporal patterns of the rainfall were significantly different and can be attributed to the boundary layer evolution. The forest produced numerous convective cells with very high rain rates mainly during the early afternoon. During the morning, the savanna built up less but still significant amounts of convective available potential energy and enough convective inhibition so that the strongest convection in the savanna did not occur until late afternoon. This timing resulted in the largest, most intense convective line of the three land covers.

1. Introduction

In this paper, we use the term ''convective line'' to refer to a multicellular convective cloud cluster in which the cumulonimbus clouds are arranged linearly. In West Africa, convective lines are typically oriented north–south and propagate westward. The term ''squall line'' will be used specifically to describe a convective line that has produced a trailing stratiform anvil. Convective line encompasses all propagating linear convective cloud clusters, whether or not they have stratiform anvils. We investigate how land cover may influence the characteristics of the boundary layer enough to produce noticeable changes in convective line development and resulting water budgets.

Currently in West Africa, grassy savanna constitutes the majority of the area in the box shown in Fig. 1. The savanna region supports millet cultivation and livestock grazing. From satellite observations of land cover in this region, changes in vegetation density are closely correlated with interannual fluctuations in rainfall, although human activity may exacerbate ecosystem changes, particularly during dry years (Nicholson et al. 1998). Hence, agricultural productivity and aquifer recharge will depend greatly on the size and other characteristics of wet season convective lines. Brubaker et al. (1993) have shown that precipitation recycling approaches 50% in West Africa in the summer, implying an important role for the land surface in rainfall development. In this study, we concentrate on examining the physical links between surface processes and boundary layer processes and their effect on convective clouds.

Wet season boundary layer temperature and humidity profiles are governed by the intrusion of humid air in the summer monsoon and the contribution from land surface evapotranspiration. Soil water content and land cover govern evaportranspiration and the flux of energy

Corresponding author address: Karen I. Mohr, Department of Earth and Atmospheric Sciences, University at Albany, SUNY, Albany, NY 12222.
E-mail: mohr@atmos.albany.edu

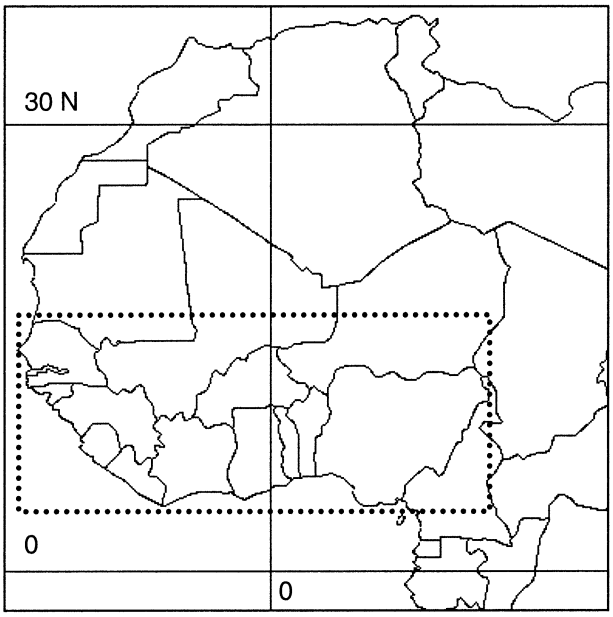


FIG. 1. Map of West Africa with political subdivisions. The box (dotted line) encloses the geographic region relevant to this study, approximately 4°–17°N, 17°W–15°E. The three land covers tested occur within this box.

and water vapor to the boundary layer. Variability in the latent heat flux may thus suppress or enhance moist convection locally. Crook (1996) and Lucas et al. (2000) have investigated the possible sensitivity of convection to environmental humidity by using cloud-resolving models. Both studies found noticeable increases in the amount of rainfall with small increases in boundary layer humidity. In Crook's (1996) study, changes in the boundary layer humidity on the order of observational error, 1 g kg^{-1}, made the difference between no initiation and intense convection.

Hydrometeorological modeling permits us to control inputs and measure outputs in land–atmosphere interaction quantitatively. The purpose is not to stimulate a particular convective line event as in a case study but to examine how model convective lines develop in different environments and isolate the factors that may be responsible for measurable differences in their water budgets. Previous studies using cloud-resolving models to simulate convective lines in West Africa have prescribed surface fluxes rather than having an interactive land surface (Dudhia et al. 1987; Lafore and Moncrieff 1989; Chang and Yoshizaki 1993; Caniaux et al. 1994). We use a coupled, fully interactive land–atmosphere (cloud resolving) model to compare convective system development over three different land covers found in West Africa: grassy savanna (SAV), semidesert (SD), and evergreen broadleaf forest (FOR). Since precipitation from a convective line is a function of system size, structure, and longevity, precipitation and associated variables in the water budget (e.g., condensation and evaporation) will be the key results used to evaluate differences among simulations.

2. Methods

a. Numerical model

The simulations for this study used a two-dimensional (2D) coupled land–atmosphere (cloud resolving) numerical model with open lateral boundary conditions. The Goddard Cumulus Ensemble (GCE) model is a nonhydrostatic, anelastic numerical cloud resolving model composed of prognostic equations for momentum, potential temperature, and water vapor mixing ratio (Tao and Simpson 1993). The GCE includes solar and infrared radiative transfer processes, a Kessler-type two-category (cloud drops and rain) liquid water scheme, and a three-category (cloud ice, snow, and graupel/hail) ice microphysics schemes (Lin et al. 1983; Rutledge and Hobbs 1984). For our simulations of tropical convection, we chose graupel as our third class of ice particles. Coupled to GCE is the Parameterization for Land–Atmosphere–Cloud Exchange (PLACE), a surface–vegetation–atmosphere transfer model (Wetzel and Boone 1995). PLACE consists of linked process models (e.g., net radiation, evapotranspiration, ground heat storage) and emphasizes the vertical transport of moisture and energy through the five-layer soil moisture and the seven-layer soil temperature column to the overlying heterogeneous land surface. The exchange of radiation and heat, momentum, and moisture fluxes couple the GCE and PLACE models (Tao et al. 2002). Lynn et al. (1998) and Barker et al. (2001) have used GCE–PLACE to simulate landscape-generated and sea-breeze-generated deep convection.

A computationally efficient 2D model such as GCE–PLACE is an attractive choice, supported by the results of previous studies that show that the time-mean kinematic and thermodynamic properties of a convective line are well simulated in 2D models (Nicholls et al. 1988; Ferrier et al. 1996; Tao et al. 1996; Xu and Randall 1996; Grabowski et al. 1998; Lucas et al. 2000). The simulation of horizontal circulation features, momentum transports, and other inherently three-dimensional features of convective line dynamics would be more appropriately handled with three-dimensional models. In this study we focus on the mean and cumulative values of surface rainfall and other hydrologic variables.

The grid used in the simulations was a transect of approximately 1000 km divided into 2048 grid points with 1990 inner points at 0.5-km spacing and a stretched (1:1.06) grid on either side. Vertically, there were 33 grid points from 0.0- to 21.5-km altitude. The grid was stretched, with spacing between levels ranging from 80 m at the surface to 1200 m at the top of the troposphere. Stretching in the vertical increases computational efficiency without significantly compromising accuracy (Weisman et al. 1997). Boundary conditions were open

lateral. The GCE time step was 5 s, and GCE invoked PLACE in 3-min intervals. All simulations began at local midnight and ran for 24 h.

b. Initial conditions

Figures 2a,b depict the sounding used to initiate simulations. This sounding is a modification of a sounding taken 23 June 1981 at 2335 UTC, during the Convection Profonde Tropicale (COPT81) field experiment in an area straddling the Ivory Coast and Burkina Faso (Chalon et al. 1988; Roux 1988). Abrupt changes of humidity, wind direction, and wind speed over a few millibars can cause numerical instability, requiring that the field-observed sounding be smoothed. Initial convective available potential energy (CAPE) of the sounding in Fig. 2a is 2895 J kg^{-1}, calculated by lifting the air from the lowest 50 mb. In the wind profile in Fig. 2b, the core of the African easterly jet is centered at 650 mb, and the core of the tropical easterly jet is centered at 120 mb. There are 2.8×10^{-3} s^{-1} low-level shear (surface to the height of the maximum low-level wind), -1.5×10^{-3} s^{-1} midlevel shear (height of maximum low-level wind to 6 km), and -6.5×10^{-4} s^{-1} deep-level shear (height of the maximum low-level wind to 10.3 km).

The initial surface conditions define the simulations used in this study. There are three land covers: semi-desert (scrub), savanna, and evergreen broadleaf forest, described in Table 1. The semidesert land cover is sparse, deeply rooted, highly reflective, and tolerant of high temperatures. The savanna and broadleaf forest land covers are noticeably thicker as well as taller, and most of the roots are higher in the soil column than in the semidesert. We will make frequent use of the abbreviations in Table 1 in referring to each simulation. All grid points in all of the simulations were assigned sandy loam soil, a common soil type in the region. Although this assumption simplifies the natural variability of soil types in the region, Mohr et al. (2000) have shown that PLACE's sensitivity to soil type can overwhelm any signal from vegetation characteristics.

In Table 1 the initial volumetric soil moisture at each grid cell varies from 0.20 cm^3 cm^{-3} (50% saturation) in the lowest layers to as little as 0.05 cm^3 cm^{-3} (12.5% of saturation) in the near-surface layers. Compared to time series of observations of soil moisture taken during the summer of 1992 in Niger (data available online at http://www.ird.fr/hapex), these profiles are moister, particularly in the lowest layers, than average for semi-desert observation sites and similar to grassland observation sites between rainfall events. It is likely the profiles are drier than average for a heavily vegetated forest area because moist soils and dense vegetation are a unified ecosystem characteristic of a tropical forest region. Because surface fluxes in PLACE are highly sensitive to initial soil moisture content in the layers where roots are concentrated (Mohr et al. 2000), we chose to minimize differences in initial soil moisture profiles to isolate as much as possible the sensitivity to vegetation. Using this approach, we are likely to find the lower bound of the sensitivity of convective lines to land sur-

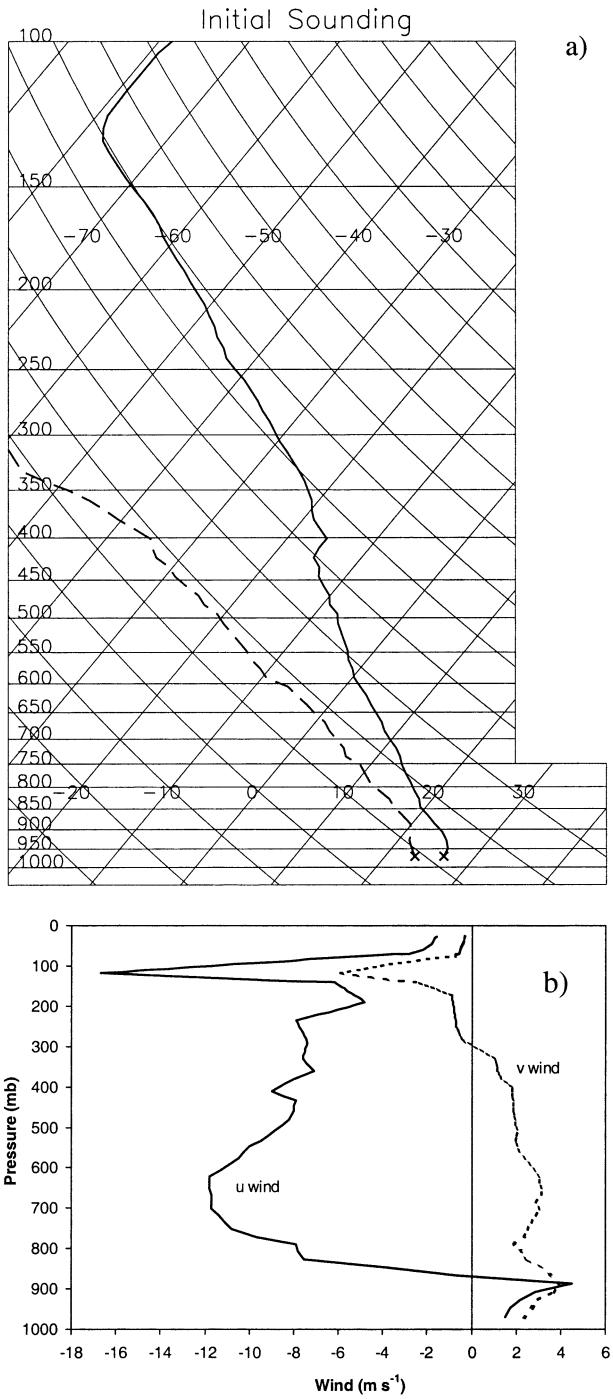


FIG. 2. (a) Sounding used to initialize simulations. Modifications to this sounding for sensitivity tests are noted in the description of the tests. (b) Wind profile used to initialize simulations. The *u* wind is the solid line, *v* wind dashed.

TABLE 1. Selected vegetation and soil characteristics for the three land covers. The % vegetation cover is the percentage of area covered by transpiring vegetation; root profile is the cumulative frequency distribution of roots in the five soil moisture reservoirs; surface roughness is in m; minimum stomatal resistance is in s m^{-1}; surface biomass (water equivalent) heat capacity is in J K^{-1} m^{-2}. For soil, saturated hydraulic conductivity is in m s^{-1}. Initial soil moisture is expressed as volumetric (cm^3 cm^{-3}) soil moisture, the ratio of the volume of soil water to total soil volume.

Vegetation	SD	SAV	FOR	Sandy loam soil	SD	SAV	FOR
Albedo	0.25	0.18	0.14	Albedo	0.20	0.20	0.20
% Vegetation cover	20%	50%	70%	Porosity	0.40	0.40	0.40
LAI	0.40	2.0	3.75	Saturated hydraulic conductivity	1.2×10^{-3}	1.2×10^{-3}	1.2×10^{-3}
Root profiles layers 1–5	0.0	0.0	0.0	Initial soil moisture layers 1–5	0.05	0.07	0.10
	0.20	0.25	0.25		0.07	0.10	0.12
	0.25	0.50	0.50		0.12	0.15	0.18
	0.50	0.25	0.25		0.15	0.18	0.20
	0.05	0.0	0.0		0.18	0.20	0.20
Surface roughness	0.05	0.20	1.5	% silt	20%	20%	20%
Min stomatal resistance	110.0	110.0	80.0	% sand	70%	70%	70%
Biomass heat capacity	0.25	1.0	5.0	% clay	10%	10%	10%

face conditions in very dry and very moist environments.

Before beginning a 24-h simulation, the soil and the atmosphere must be in quasi equilibrium to avoid generating large nonphysical surface fluxes. We created first-guess soil moisture and soil temperature profiles and ran PLACE offline, forced by the temperature, pressure, and wind speed in the lowest levels of the sounding (Fig. 2). We assumed that the basic state variables in the nocturnal surface layer would not change significantly from midnight to 0300 local time. The final soil moisture and soil temperature profiles at the end of the first 3-h offline simulation became the initial soil moisture and soil temperature profiles for a repeat of the 3-h simulation. The 3-h simulation was repeated until the initial and final soil moisture profiles were nearly identical (about 50 times). This methodology was applied to each of our three land covers, so that each land cover had its own initial soil moisture and soil temperature profiles (Table 1).

Previous studies using COPT81 soundings to model squall lines on 22 or 23 June 1981 used either a cold pool (Lafore and Moncrieff 1989; Caniaux et al. 1994; Liu et al. 1997) or warm bubble (Chang and Yoshizaki 1993) to initiate convection. In the absence of significant orography, strong storms are typically triggered by distinct thermal boundaries such as sea breezes or drylines. A cold pool or warm bubble is the cloud modeler's makeshift thermal discontinuity. Such a trigger permits a large cell to initiate in a particular location in the domain and evolve almost from the beginning of the simulation into a single large, well-organized squall line. Thus, the COPT81 soundings are truly the prestorm environment soundings for the previously mentioned studies. Since we are attempting to isolate the sensitivity of convective initiation and development to land surface conditions, we do not apply a lifting mechanism, instead allowing the initial sounding in Fig. 2 to evolve over the course of a day. What form of organized convection will result from triggering by surface heating gradients during an active summer monsoon?

c. Observations of convective clusters during an active monsoon

Unlike the previous studies using COPT81 data, our prestorm environment arises from a COPT81 sounding modified by 12 h of interaction with the surface. Because of the marked differences in experimental design between our study and the previous COPT81 modeling studies, our results are more appropriately compared to weather typical of West Africa during an active monsoon in late June. Observations obtained from microwave remote sensing can provide insight into the size, intensity, and geographic distribution of convective clusters during an active monsoon. Since the COPT81 period was not observed by a microwave sensor, we will consider a representative period, 26–30 June 1998, cov-

ered by the Tropical Rainfall Measuring Mission (TRMM) Microwave Imager (TMI). Historical reanalysis data for this time period (plots available online at http://www.cdc.noaa.gov/HistData) reveal coincident westerly zonal wind and negative outgoing longwave radiation anomalies, indicating significant convective activity. Each day during this time period, the TMI observed the eastern two-thirds of the box in Fig. 1 (i.e., 4°–17°N, 5°W–15°E) in the late afternoon when convective activity peaks.

Choosing an 85-GHz brightness temperature contour of 255 K to distinguish between raining cloud and clear air and/or nonprecipitating cloud (Prabhakara et al. 2000), the contour plots in Fig. 3 show numerous small convective clusters scattered across the TMI swaths. Small convective clusters with less than 1000 km^2 of precipitating cloud (fewer than 10 cumulonimbus clouds) constituted 90% of the total number of convective clusters (504) sampled by TMI in 15 overpasses of the region bounded by 4°–17°N, 5°W–15°E. The majority of precipitating cloud clusters consisted of one–two cumulonimbus clouds and they developed every day. During this 5-day period, only seven squall lines developed, occurring on 27, 28, and 30 June. Although further study is needed, it appears more likely that multiple small convective lines rather than a single large squall line will develop from daytime heating of the potentially unstable boundary layer during an active West African monsoon.

3. Results

a. Heat fluxes and boundary layer energy

Equation (1) is the PLACE-calculated surface energy budget applicable to the vegetation layer at the air–ground interface:

$$b_M \frac{\partial T_S}{\partial t} = R_{\text{net}} - G - E - H. \quad (1)$$

The left-hand side of Eq. (1) represents the effect of energy storage by biomass. The water-equivalent heat capacity of the biomass is b_M (J K^{-1} m^{-2}). On the right-hand side are the surface flux terms, net radiation (R_{net}), heat flux into the soil (G), latent heat flux (E), and sensible heat flux (H).

The time series of surface fluxes are plotted in Fig. 4. Simulation hours correspond to local times (midnight = hour 0). Net radiation is strongly dependent on surface albedo (Table 1). Figure 4a is the area-average difference between net radiation and ground heat flux ($R_{\text{net}} - G$) for the SD, SAV, and FOR land cover simulations. The comparison of net radiation to the ground heat flux indicates the fraction of radiation conducted into the soil versus the fraction available to affect the diurnal cycle of low-level equivalent potential temperature (θ_e) and thus moist entropy (Betts and Ball 1995, 1998). Midday, there is 20% more available energy in the FOR simulation than in the SAV simulation and 30% more than in the SD simulation. Enhanced ground heat flux causes the SD soil temperatures to increase more rapidly than the FOR soil. The SD average 10-cm soil temperature increases 9 K and the skin temperature increases 24 K between hours 8 and 14. For the same period in the FOR, the 10-cm soil and skin temperatures increase 4 and 12 K, respectively. The highly reflective SD surface received the least net radiation, and the soil temperatures imply that a greater fraction of the radiation received was conducted into the soil.

The differences in sensible and latent heat fluxes among simulations are even larger. The midday sensible heat flux (Fig. 4b) in the SD and SAV is nearly double that of the FOR. In Fig. 4c, there are two peaks in the latent heat flux. Evapotranspiration produces the first peak in the morning, but the second peak in the afternoon has a large contribution from evaporating rainfall. In both cases, the latent heat flux in the FOR simulation is more than double than the latent heat flux in the SD and SAV simulations. For PLACE, latent heat flux is determined by plant physiology, available moisture, and atmospheric demand. High morning soil temperatures, as in the SD simulation, will suppress evapotranspiration, increase the sensible heat flux, and may establish a negative feedback between soil temperature and additional evapotranspiration (Mohr et al. 2000). Most of the available energy in the sparsely vegetated SD was converted into sensible heat flux until midafternoon. Conversely, the thickly vegetated, least-reflective FOR simulation had more available energy and converted more of it into evapotranspiration and latent heat flux throughout the day. Although the SAV has 30% more vegetation than the SD, the differences between the SAV and SD flux time series are much smaller than between the SAV and FOR time series.

The moist static energy (MSE), or moist entropy, in the boundary layer is the sum of the potential energy, sensible heat energy, and latent heat energy. The MSE is easily related to surface fluxes and is useful for diagnosing the thermodynamic state of the boundary layer:

$$\text{MSE} = gz + C_pT + Lw. \quad (2)$$

Here, g is the gravitational acceleration, z elevation, C_p specific heat capacity at constant pressure, T temperature, L latent heat of vaporization, and w water vapor mixing ratio. Of these terms, the sensible heat term is the largest, on the order of 10^5 J kg^{-1}, and the latent heat term an order of magnitude smaller. A significant vertical gradient of MSE encourages the development of moist convection to reestablish a neutral vertical distribution. The vertical gradient of MSE can be diagnosed by using equivalent potential temperature (θ_e) as a proxy. In Fig. 5a, the FOR has a uniform 0.5-km layer of air with θ_e greater than 348 K, and much of the surface layer is greater than 352 K. Below 0.5 km the SAV (Fig. 5b) varies from 346 to 352 K, with isolated patches above 350 K. The SD (Fig. 5c) has only isolated

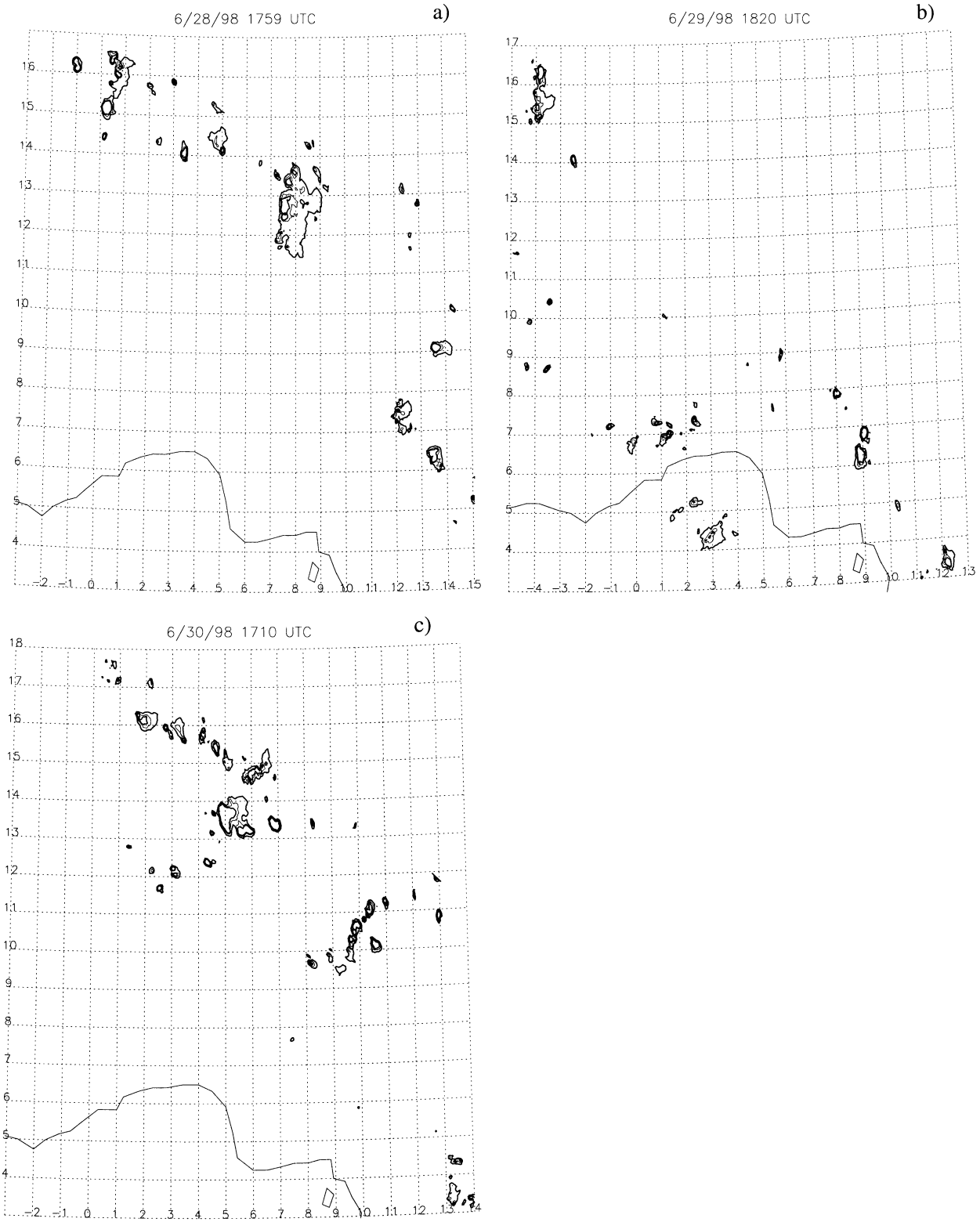


FIG. 3. Contour plots of 85-GHz brightness temperature from the TMI for three times in Jun 1998: (a) 1759 UTC 28 Jun, (b) 1820 UTC 29 Jun, (c) 1710 UTC 30 Jun. Overpass times are noted. The contours are 255, 225, and 200 K, where 255 K separates raining from nonraining cloud, 225 K denotes the presence of convective cloud, and 200 K denotes strong convection.

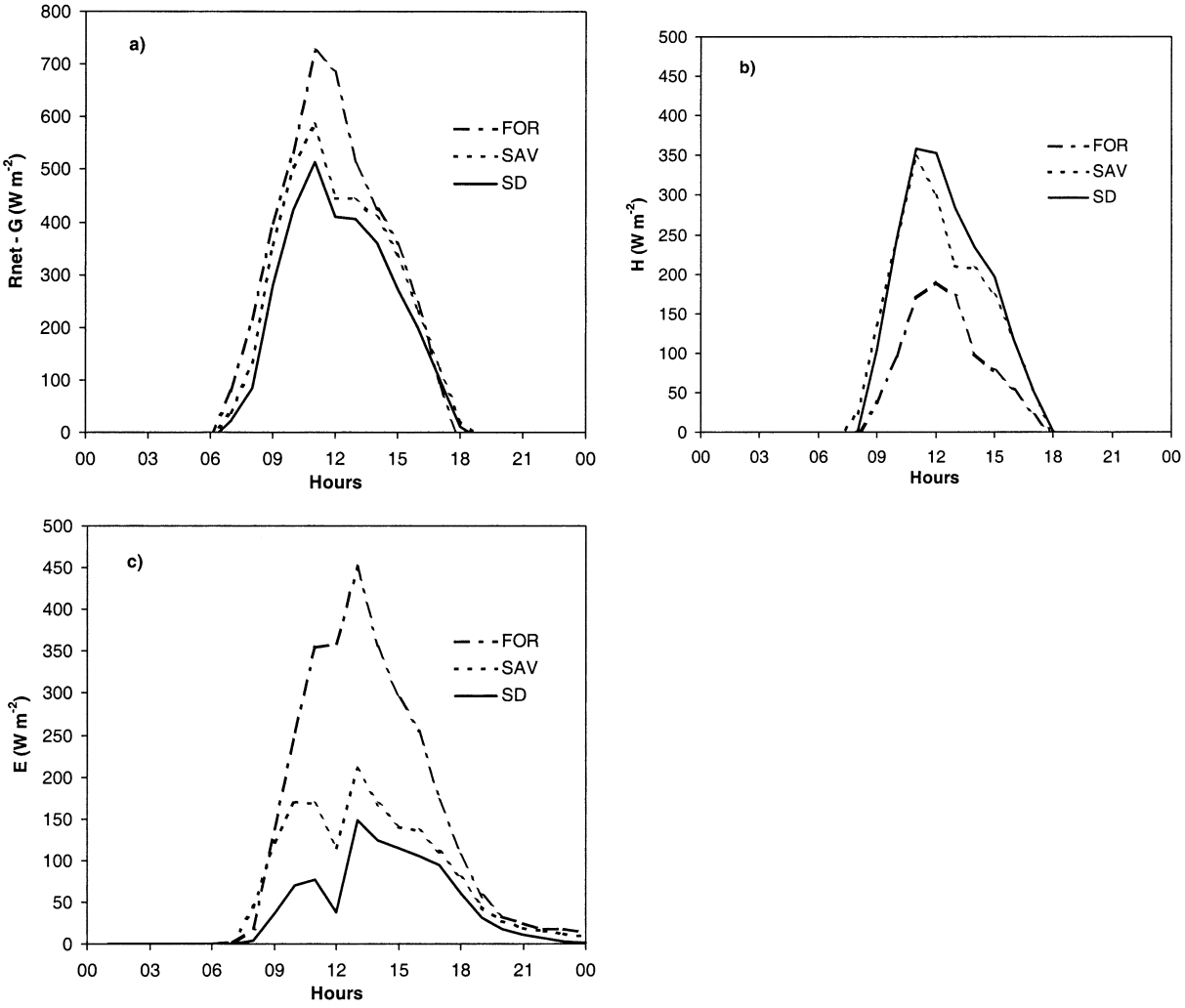


FIG. 4. Time series of domain-average surface fluxes: (a) available energy ($R_{net} - G$), (b) sensible heat, (c) latent heat.

patches greater than 348 K. Below 1.5 km, the FOR simulation has the largest vertical gradient of θ_e.

Related to differences in the vertical MSE/θ_e gradient are differences in boundary layer growth and mixing ratio since all are affected by surface fluxes. Because all simulations used the same initial sounding, the boundary layer height and mean mixing ratio in the boundary layer is very similar until sunrise. The boundary layer growth from sunrise to noon was faster and deeper in the SD simulation, attaining a maximum height of 1.56 km. The SAV boundary layer also reached 1.56 km but more slowly than in the SD. The FOR boundary layer maximum height was one model layer shallower (1.21 km). During the morning, the mixing ratio in the shallower FOR boundary layer was consistently 2–3 g kg^{-1} (~20%) higher than the SAV and SD. Although the FOR simulation had the smallest sensible heat term (C_pT) in Eq. (2), the contribution by evapotranspiration to the latent heat term (Lw) coupled with a shallower boundary layer resulted in the FOR having the highest moist static energy density in the boundary layer by noontime.

A more conventional measure of the potential for deep convection is CAPE. By noon, the FOR had 3720 J kg^{-1} of CAPE, 13% more than the SAV (3240 J kg^{-1}) and 27% more than the SD (2730 J kg^{-1}). The SD simulation had less CAPE than the others throughout the simulation period. Based on the environmental characteristics discussed in this section, by noontime the FOR was the most likely to produce heavy rainfall and the SD the least.

b. Cloud and system development

Around noon, enhanced cumulus began forming in all three environments across the model domain. To assess convective intensity, Fig. 6 is the time series of the peak updrafts in the convective cores. The peak vertical velocity in the FOR simulation is consistently near or above 15 m s^{-1} for hours 12–17. The strongest updrafts

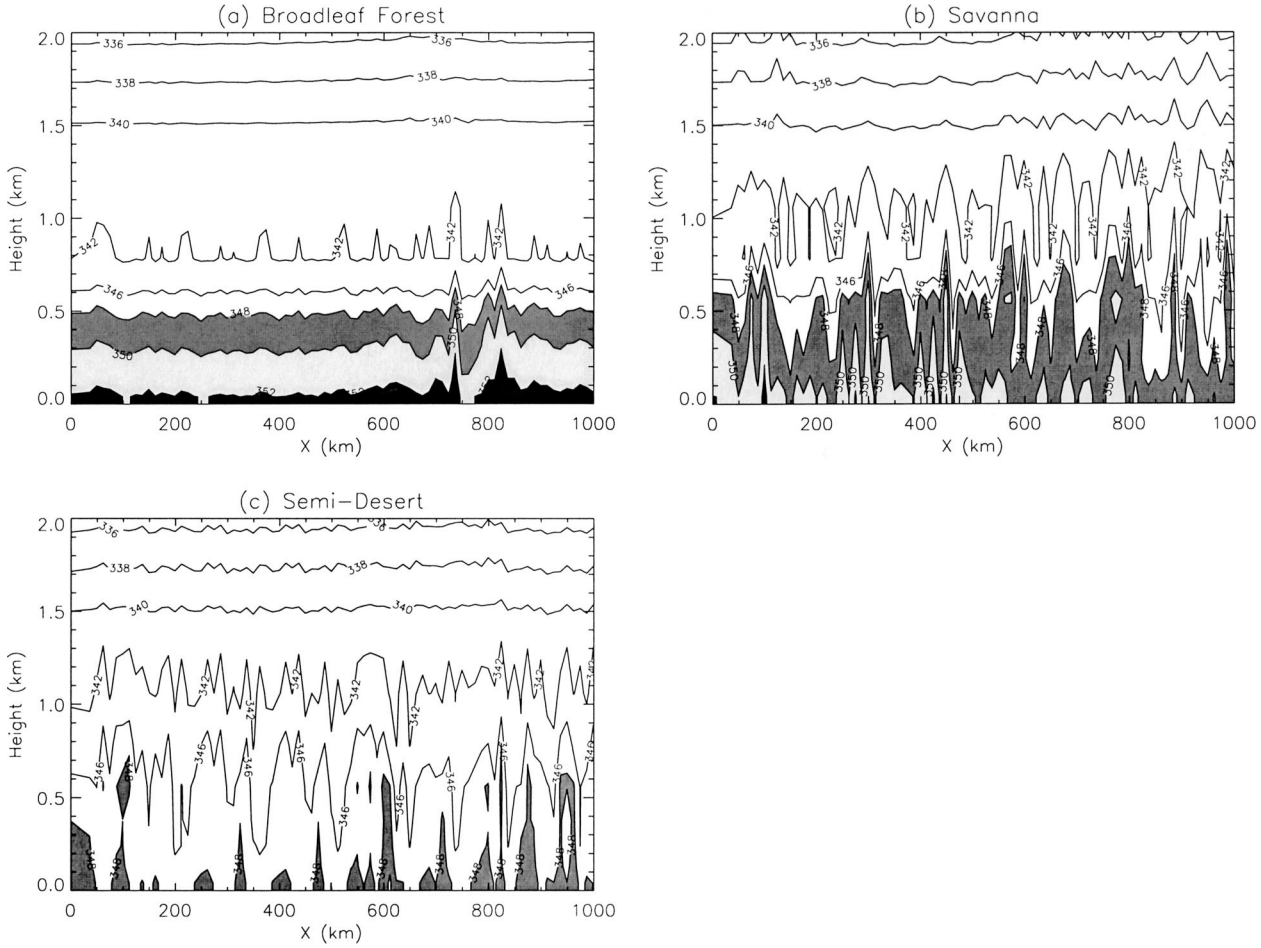


FIG. 5. The x–z contour plots of θ_e at hour 11 for (a) FOR, (b) SAV, (c) SD. The 348-K contour is shaded dark gray, 350-K contour shaded light gray, 352-K contour shaded black.

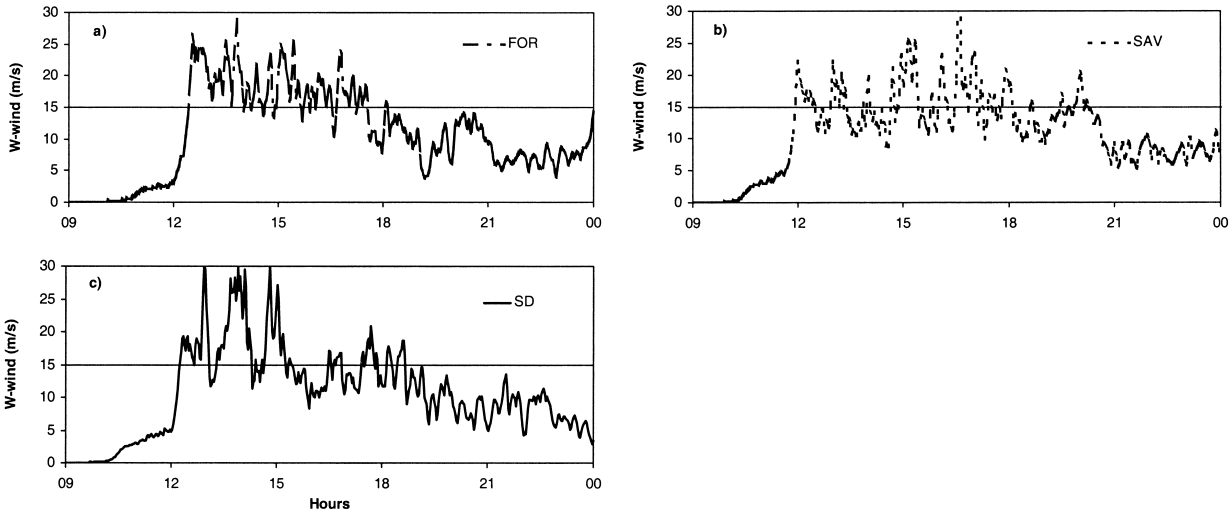


FIG. 6. Time series of the peak updrafts in the convective cores for (a) FOR, (b) SAV, (c) SD. Updrafts are 1 m s^{-1} or greater for at least 500 m (one grid cell).

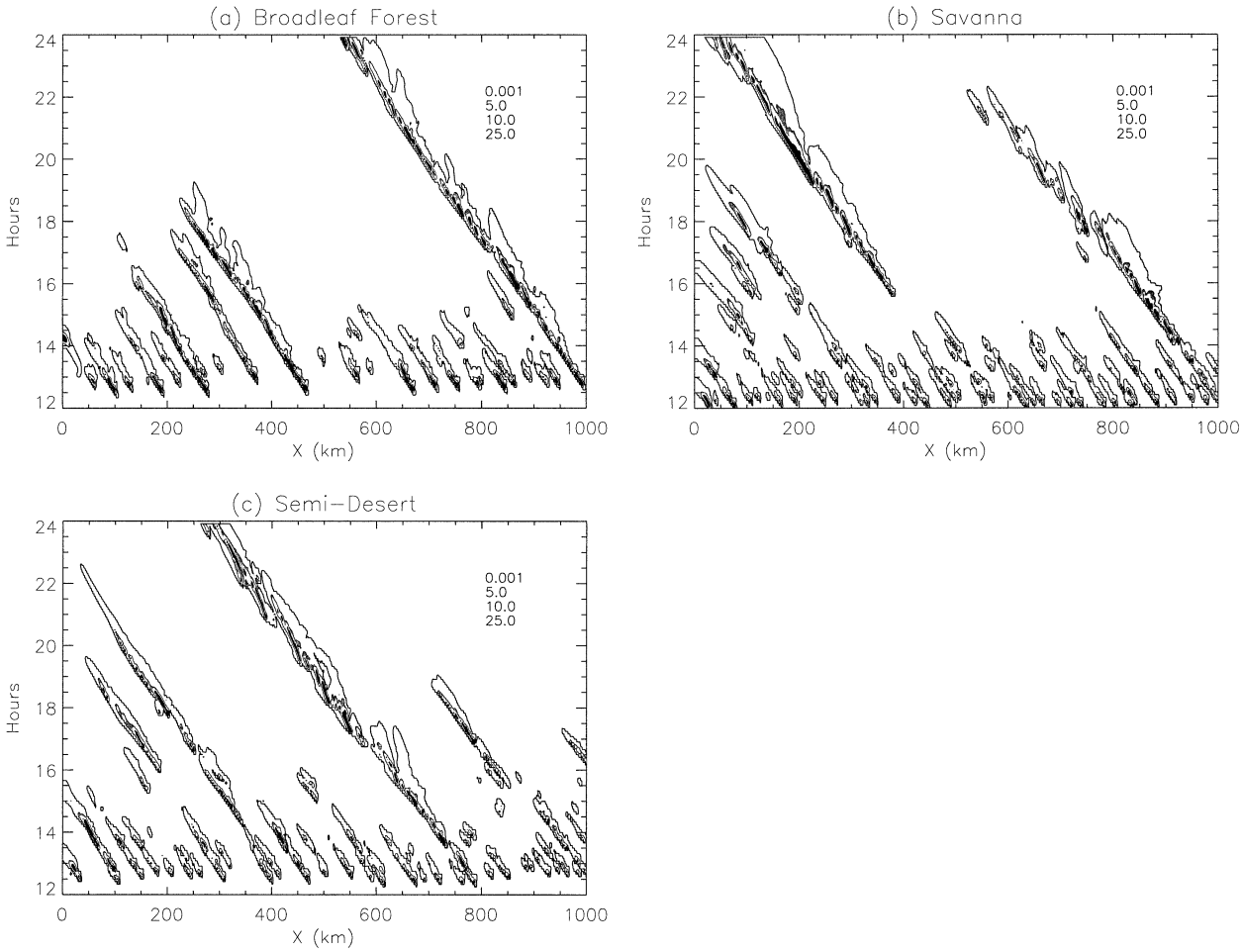


FIG. 7. The *x–t* plots of surface rainfall rates for (a) FOR, (b) SAV, (c) SD. The 5.0 mm h^{-1} contour is shaded dark gray, 10.0 mm h^{-1} contour shaded light gray, 25.0 mm h^{-1} contour shaded black.

in the SAV simulation do not develop until the midafternoon, and only the SAV has a peak greater than 15 m s^{-1} after hour 19. The SD simulation has strong but less consistently intense updrafts than the FOR. The longest sustained updraft in the SD at or above 15 m s^{-1} is 40 min between hours 13.5 and 14.5. The peak updraft is declining in the SD by the end of the simulation period whereas the SAV and FOR averages are the same or increasing.

The *x–t* plots of rainfall in Fig. 7 provide a life history of the convective lines in the three simulations. Over the course of the afternoon in all three simulations, most of the convective cells dissipated, but a few cells developed outflow sufficient to trigger new cells. Hence, small convective lines developed in all of the simulations. Although fewer convective lines initiate in the FOR simulation than in the SAV and SD simulations, nearly all of the FOR lines have intense rainfall (>25 mm h^{-1}). For the FOR convective lines initiating at 1000, 450, 400, and 300 km, the intense rainfall occurs over the course of several hours, although only the convective line initiating at 1000 km has intense rainfall past 18 h. Intense rainfall is more limited in time and space in the SD simulation with only one convective line remaining by the end of the simulation period. The SAV simulation generates more convective lines initially even though most lack heavy rainfall. The most important feature of the SAV simulation is the squall line that initiates at 400 km at 16 h. This is the largest convective line produced in any simulation, and it has the most extensive area (time and space) of intense rainfall. By the end of the simulation, its stratiform region is nearly 150 km wide, comparable to the stratiform region of the squall line at 13°N, 8°E in Fig. 3a (28 June), but smaller and less well developed than the stratiform regions in the COPT81 squall-line case studies.

In Fig. 8 are time–height plots of domain average suspended condensate (units of 10^8 kg km^{-1} for consistency with water budgets discussed later). The suspended condensate is the sum of the masses of cloud liquid water, cloud ice, snow, rain, and graupel. The most rapid accumulation of condensate occurred during

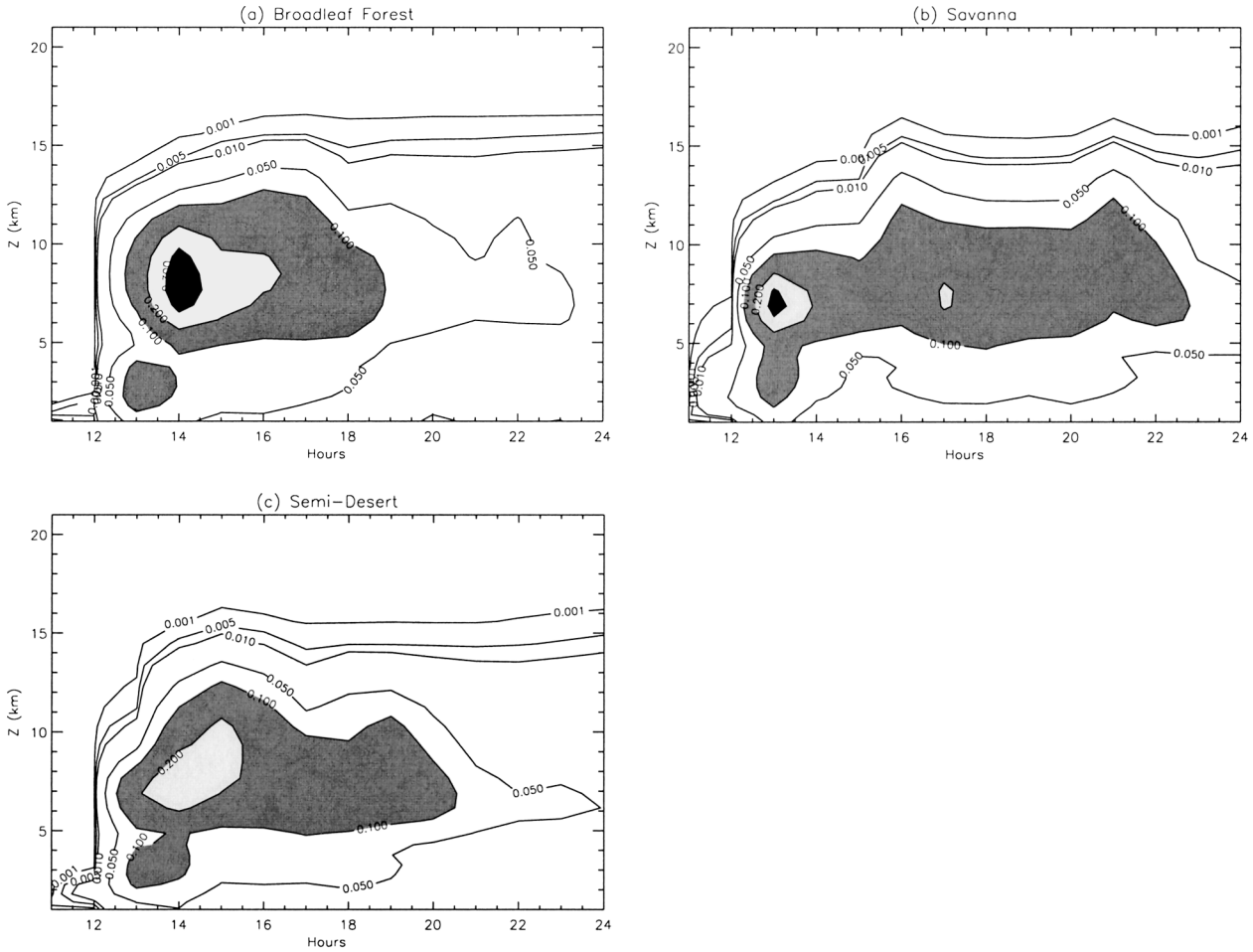


FIG. 8. The *t*–*z* plots of domain average suspended condensate (10^8 kg km^{-1}) for (a) FOR, (b) SAV, (c) SD. The 0.100 contour is shaded dark gray, 0.200 contour shaded light gray, 0.300 contour shaded black.

the peak extent of cloud cover 1–2 h after initiation of enhanced cumulus, when the number of convective cells was at a maximum and the updrafts (Fig. 6) were most likely to be 15 m s^{-1} or more. The FOR simulation produced the most condensate in the deepest layer through hour 18, but the SAV simulation produced significantly more condensate than the other simulations after hour 18. The surface rainfall patterns are consistent with the production of suspended condensate. The exact percentages of precipitating area at particular surface rainfall rates are in the cumulative frequency distributions for surface rainfall in Table 2. The FOR simulation has a greater percentage of area with intense rainfall than the SD and SAV, with most of that occurring in the first 3–4 h after initiation, according to Fig. 7. The SAV has the smallest percentage of intense rainfall, and most of it occurs after 18 h in its largest convective line. The stratiform area of the SAV squall line skewed the distribution in Table 2 to the left. Figures 6–8 and Table 2 confirm that differences in boundary characteristics during the morning over the three different land covers produced appreciable differences in convective development.

TABLE 2. Cumulative frequency distributions for surface rainfall rates (mm h^{-1}).

Land cover	0–5	5–10	10–25	25–50	50–100	>100
SD	82.0%	6.4%	6.3%	3.1%	1.6%	0.6%
SAV	83.8%	5.6%	5.5%	2.7%	1.6%	0.8%
FOR	80.8%	5.5%	6.1%	3.6%	2.6%	1.4%

The budget of condensed water integrated over time over the full model domain is

$$C = E + R + S_c, \tag{3}$$

where C is the total condensation plus the total deposition, E the total evaporation plus the total sublimation, R the total surface rainfall, and S_c the mass of suspended condensate. The precipitation efficiency (PE) is defined as

$$\mathrm{PE} = \frac{C}{R}. \tag{4}$$

Table 3 is the final water budget for the SD, SAV, and

TABLE 3. Final water budgets for the three land covers. Units for C through S_c are 10^8 kg km^{-1}.

Simulation total	SD	SAV	FOR
C	121.83	136.55	122.50
E	76.60	85.03	70.90
R	37.52	45.63	45.68
S_c	7.70	5.89	5.93
PE	0.31	0.33	0.37

FOR simulations. The FOR has almost the same surface rainfall as the SAV (22.9 vs 22.8 mm per grid cell) despite having 10% less total condensation. Table 3 obscures the history revealed by Figs. 7 and 8. The FOR simulation produced 60% of its total condensation between hours 12 and 15. In this period, the SAV had produced 40% of its total condensation, producing the remaining 60% after hour 18. The FOR simulation evolved more rapidly as well as more efficiently converted condensate to rainfall. The SD and FOR had comparable total condensation, but the lower precipitation efficiency and higher mass of suspended condensate of the SD imply that more nonraining cloud cover was produced. The SD produced 18.8 mm of rainfall per grid cell, 18% less than the SAV and FOR.

c. Discussion of the land–atmosphere interaction

Given the same sounding and similar initial soil moisture and temperature profiles for the three land covers, Figs. 4 and 5 imply that, for the FOR simulation, evapotranspiration from the forest cover helped to create a moister boundary layer with more CAPE, a stronger vertical gradient of θ_e, and a higher MSE density during the morning hours. A moist boundary layer has a smaller humidity gradient between environmental air and air in the convective updrafts, so that entrainment is less effective in evaporating moisture in the updrafts. A high CAPE permits significant vertical cloud growth. Potentially more rainfall and colder downdrafts can then be produced and at a faster rate. Figures 7 and 8 hint at the efficiency of the production of rainfall in the FOR simulation. In Table 3, the FOR produces 10% less condensation but 17% less evaporation than the SAV and slightly more condensation but 8% less evaporation than the SD.

If conditions in the FOR simulation favored strong convection and heavy rainfall for a 4-h period in the early afternoon to midafternoon, why did the SAV simulation initiate the strongest convective line in the late afternoon? At noon, the SAV simulation had less CAPE than the FOR (3240 vs 3720 J kg^{-1}, 13% less) and twice as much convective inhibition (CIN). The SAV had 28 J kg^{-1} of CIN versus 11 J kg^{-1} for the FOR. Increased entrainment in the higher, drier SAV boundary layer would result in fewer of the early convective lines having intense rainfall. Figure 9 contains time–height plots of domain average θ_e. The burst of strong convection in the FOR reduced the θ_e gradient on the left-hand side of Fig. 9a, so that by 18 h, very little of the warm air produced during the morning remains. The SD simulation (Fig. 9c) did not have a very strong θ_e gradient by noontime, and the strong cells that were able to develop eliminated it by 18 h as well.

Boundary layer height and CIN both act to screen out weaker convective cells, such that only the strongest few are able to achieve deep penetration. Destabilization of the boundary layer and/or mechanical triggering are required to assist parcels in reaching their level of free convection. In the late afternoon, the SAV (Fig. 9b) had a large bubble of relatively warm air and an appreciable θ_e gradient. Not only did the SAV still have substantial CAPE (1120 J kg^{-1}), but the CIN increased very little (28 J kg^{-1} at noon to 34 J kg^{-1}) also. In comparison, CIN in the FOR simulation had increased to 66 J kg^{-1}. The less intense early afternoon convection in the SAV resulted in less modification of the SAV environment. By the late afternoon, maximum surface temperatures (maximum destabilization of the boundary layer by surface heating) coincided with an environment favorable to the initiation of new convection. In contrast, both the FOR and SD simulations had high CIN and no MSE/θ_e gradient to invite convective initiation outside of the influence of already propagating disturbances. The capping effect of the morning CIN and the higher, drier (but not too dry) SAV boundary layer appears to have made possible the late afternoon initiation of a squall line.

4. Sensitivity testing

Thus far, we have compared the effect of different land covers on boundary layer characteristics and surface rainfall. An important issue is the relative importance of particular initial conditions related to land cover. This is not an exhaustive sensitivity study of all the possibilities in the West African environment. A few important initial conditions are discussed—initial sounding humidity and selected vegetation characteristics—to assess their effect on the timing and magnitude of surface rainfall.

a. Initial sounding humidity

How does changing the landscape and thus local evapotranspiration compare to changes in the sounding that might be caused by changes in the summer monsoon and the transport of water vapor? We conducted four additional simulations using the savanna land cover to which we added 2% and 5% to the observed mixing ratios at all levels in the original sounding and then subtracted 2% and 5% from the original sounding. Inspection of sounding data from Dakar, Senegal, suggests that 2% and 5% are within the range of variability in humidity in the West African summer monsoon. Table

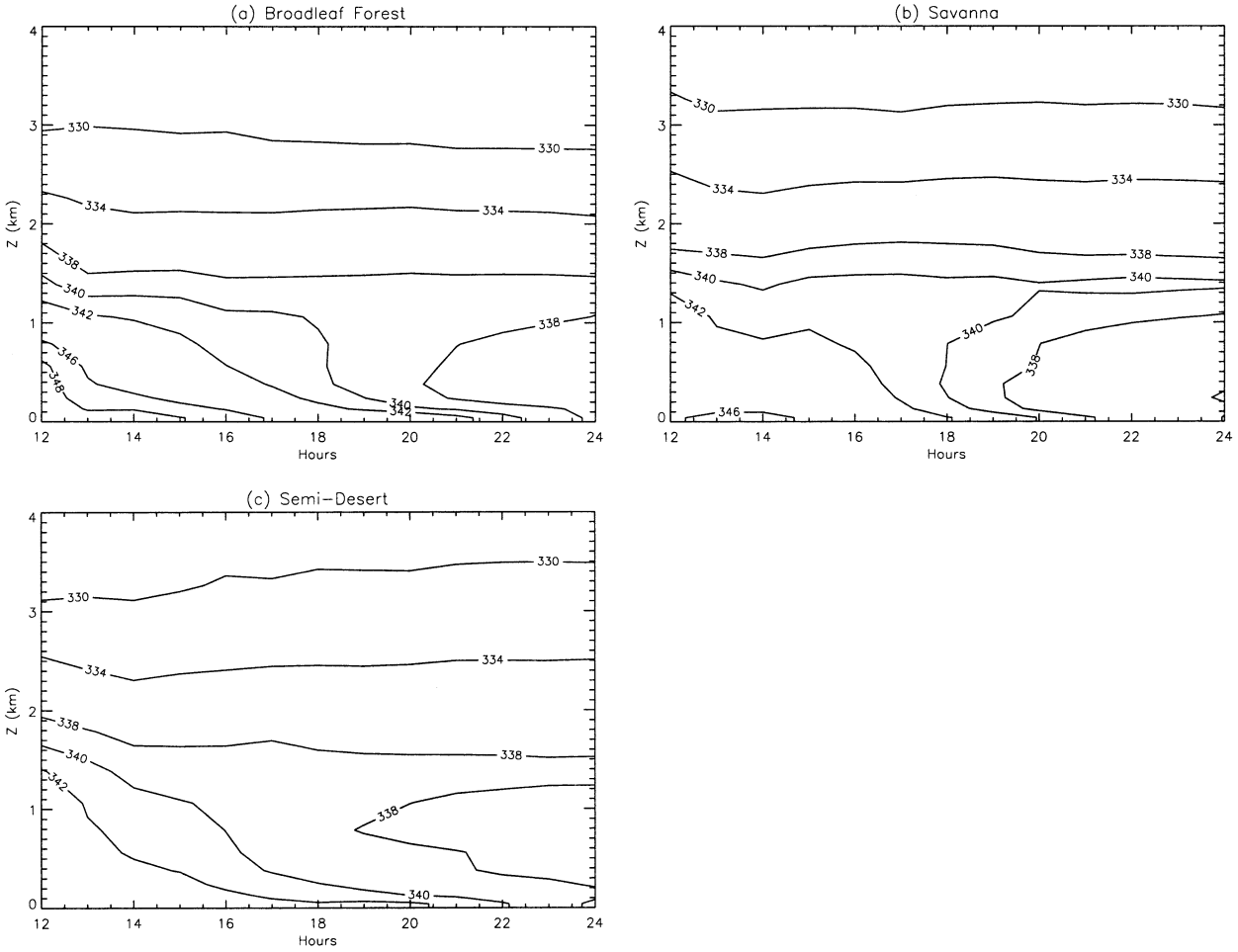


FIG. 9. The *t*–*z* plots of domain average θ_e (K) for (a) FOR, (b) SAV, (c) SD.

4 contains the final water budgets of these tests with the original SAV simulation as the control. Increasing the humidity increased the rainfall by 5% and 14% for the +2% and +5% simulations, respectively. Decreasing the humidity had a greater impact than increasing it. The rainfall decreased by 17% and 30% for the −2% and −5% simulations, respectively. In the minus simulations, the amount of total condensation decreases significantly whereas total evaporation does not. Entrainment of increasingly drier environmental air decreased the upward mass flux in the convective updrafts from the control to the −5% simulation.

For the sake of brevity, *x*–*t* plots of rainfall are not included here, but it is worth summarizing what they reveal. A late-afternoon squall line developed only in the +2% simulation, and it was smaller and shorter lived than the squall line in the control SAV simulation. The minus simulations appear to have lacked the right late-day combination of CAPE and CIN, producing less than 1000 J kg^{-1} CAPE and more than 50 J kg^{-1} of CIN. As in the FOR simulation, the +5% simulation produced strong convection early on and modified its environment to the point only one convective line was left after hour 18. Although evapotranspiration rates increased to respond to the increased demand by a drier atmosphere, it was not enough to compensate for the loss of transported water vapor represented by the minus simulations.

b. The effect of selected land cover parameters

Which vegetation characteristics in Table 1 produce a measurable effect on convection and rainfall? Table 5 lists the sensitivity tests on selected vegetation and soil characteristics. The ''plus'' and ''minus'' refer to simulations where the selected parameter was more or less than the control SAV simulation. Sensitivity test 7 considers the effect of subgrid variability of soil moisture. The control SAV simulation applies a single value of soil moisture to each grid cell, and evapotranspiration is calculated based on that water availability. To represent the variability of soil moisture within a PLACE grid cell (subgrid variability), the user designates a co-

TABLE 4. Water budgets for the humidity sensitivity tests. Units for C through S_c are 10^8 kg km^{-1}. The % change refers to surface rainfall compared to the SAV control.

Simulation total	SAV control	+2%	+5%	−2%	−5%
C	136.55	138.98	146.15	122.15	120.75
E	85.03	84.65	86.30	81.23	84.30
R	45.63	48.16	53.23	37.84	31.99
S_c	5.89	6.17	6.62	3.08	4.46
PE	0.33	0.35	0.36	0.31	0.26
% change		5%	14%	17%	30%

TABLE 5. Sensitivity tests on selected vegetation/soil characteristics. Units are the same as in Table 1; CV is the coefficient of variation, the ratio of the standard deviation of soil moisture to the mean soil moisture. See Table 1 for the differences in root distribution between the SAV and SD land covers.

Sensitivity test	Control	Minus	Plus
1) Albedo	0.18	0.10	0.24
2) % vegetation cover	50%	20%	70%
3) Min stomatal resistance	110.0	70.0	150.0
4) Surface roughness	0.2	0.05	1.0
5) LAI	2.0	1.0	3.0
6) Roots	SAV roots	SD roots	
7) Soil moisture subgrid variability	None	CV = 0.30	

efficient of variation (CV), the ratio of the standard deviation of soil moisture to the mean soil moisture.

The CV can be considered the variability relative to the amount of soil water present. If CV $>$ 0.0, PLACE derives the shape of the normal distribution from the CV, calculates the evapotranspiration at discrete values of soil moisture along the distribution, then executes a weighted average to find the grid cell evapotranspiration. In a case study of the evolution of soil moisture in a mesoscale watershed in Oklahoma, Mohr et al. (2001) found that simulations with and without subgrid variability produced very different soil moisture and surface flux gradients during dry conditions. It is worthwhile to evaluate the effect of the subgrid variability option and see if it compares to the effect of changing vegetation characteristics. A CV of 0.30 was chosen, a value representative of (mainly) dry soil with high soil moisture variability in Mohr et al. (2001).

Table 6 contains the water budgets for the sensitivity tests involving albedo, percent vegetation cover, leaf area index, root distribution, and the CV of soil moisture. These tests produced changes in the surface rainfall mass of 1% or greater. The sensitivity tests of minimum stomatal resistance and surface roughness are not included because they failed to meet this criterion.

Increasing (decreasing) the albedo decreased (increased) the surface available energy and thus the latent heat flux around 10% (around 10%). This resulted in a temporal and spatial pattern of surface rainfall similar to the SAV (Fig. 7b) with slightly less (more) rain from increased (decreased) entrainment. Changing the vegetation cover produced two interesting results. Decreasing the vegetation cover to 20% decreased the latent heat flux 50% and produced a temporal and spatial pattern of surface rainfall more similar to the SD than the SAV. When vegetation was increased to 70%, latent heat flux increased 20%. The total evaporation decreased more than the total condensation and PE and thus surface rainfall increased modestly. Similar to the SAV +2% humidity experiment, a late afternoon squall line developed, but it was smaller and shorter-lived than the squall line in the SAV control. Changes in the leaf area index exhibited the same trend as changing the percent vegetation cover, but with a smaller magnitude change in surface rainfall. Changing the total area covered by biomass had more influence over the latent heat flux and surface rainfall than changing the leaf density of the plants already there.

The root distribution directly affects the evapotranspiration rate in supply-limited conditions. The SD root distribution places more roots in the lowest and moistest soil layers, permitting SD plants to continue transpiring when SAV plants may not. Giving the SAV vegetation cover a deeper root distribution did indeed increase the latent heat flux on the order of 10%. The magnitude of the change in surface rainfall was comparable to changing the leaf area index.

All of the sensitivity tests of vegetation characteristics produced a SAV-like surface rainfall pattern, with variations in the strength and longevity of the late day convection. Setting a CV changed the surface rainfall the least, but it increased the latent heat flux the most, 35%. More importantly, it changed the temporal and spatial pattern of surface rainfall from a SAV-like pattern with strong late afternoon convection to a more FOR-like pattern with intense convective lines in the early afternoon. Even so, the SAV vegetation with a CV specified still could not exactly match the FOR. There are not as many intense early afternoon convective lines. Strong convection (updrafts $\sim$15 m s^{-1}) extends later into the afternoon, producing more total condensation and evaporation (PE lower) than the FOR.

When does changing the vegetation characteristics cause a switch over to an FOR surface rainfall pattern? The soil moisture CV sensitivity test suggests that the latent heat flux must be boosted significantly. We ran a series of simulations, in which the first set the albedo to the FOR value (0.14); the next had the FOR albedo and the FOR minimum stomatal resistance; the next added the FOR leaf area index; the last added the FOR percent vegetation cover. While the intensity of early afternoon convection increased and the intensity of late afternoon convection decreased, the changes were small until the vegetation cover was added. Only then a FOR rainfall pattern with a similar timing and relationship between condensation–evaporation–PE emerged. The sensitivity tests with percent vegetation cover suggest that just changing the vegetation cover is not enough. It is the combination of low albedo and thick cover by

TABLE 6. Final water budgets of selected sensitivity tests; ''M'' and ''P'' refer to minus and plus tests in Table 5. Units for C through S_c are 10^8 kg km^{-1}.

	Control	Albedo		% vegetation cover		LAI		Roots	CV
	SAV	1 M	1 P	2 M	2 P	5 M	5 P	6	7
C	136.55	138.50	134.13	126.95	130.08	129.72	133.37	134.83	128.85
E	85.03	85.35	83.94	81.74	74.57	80.93	79.91	81.73	76.75
R	45.63	47.10	44.68	39.74	48.61	43.05	47.13	46.93	46.14
S_c	5.89	6.05	5.51	5.48	6.90	5.73	6.33	6.17	5.96
PE	0.33	0.34	0.33	0.31	0.37	0.33	0.35	0.35	0.36
% change		3%	−2%	−13%	6%	−6%	3%	3%	1%

leafy plants that produces enough latent heat flux to create an environment capable of rapid release of CAPE early in the afternoon.

5. Conclusions

This study used a two-dimensional coupled land–atmosphere (cloud resolving) model to investigate the influence of land cover on the water budgets of convective lines in West Africa. A 2D model is both computationally efficient and capable of capturing the time-mean kinematic and thermodynamic properties of a convective line, making it useful for a study requiring a large number of simulations. We created three different land covers: a sparsely vegetated semidesert, a grassy savanna, and a dense evergreen broadleaf forest. Differences in initial soil moisture profiles were minimal to isolate as much as possible the sensitivity to vegetation. The latent heat flux, boundary layer mixing ratio, and MSE in the boundary layer exhibited noticeable variations among the three land covers. The forest had the highest latent heat flux, the shallowest, moistest, slowest growing boundary layer, and more MSE per unit area than the savanna and semidesert. The differences between the savanna and semidesert were smaller than the differences between the forest and the savanna.

Although the savanna and broadleaf forest environments produced virtually the same rainfall mass, the spatial and temporal patterns of the rainfall were significantly different. These differences can be attributed to the boundary layer environments that evolved during the morning hours. The forest boundary layer developed very high CAPE and very little CIN so that by noontime, enough destabilization of the boundary layer by daytime heating had taken place to release the CAPE. The forest produced numerous convective cells with very high rain rates mainly during the early afternoon. The semidesert's boundary layer was too dry to nurture many strong cells, resulting in 18% less rainfall than in the savanna or forest simulations. During the morning, the savanna built up less but still significant amounts of CAPE and enough CIN so that the strongest convection in the savanna did not occur until late in the afternoon when surface heating was at its daytime maximum. This timing resulted in the largest, strongest convective line of the three land covers.

Sensitivity testing of initial sounding humidity and selected vegetation characteristics in the savanna provided insight into the importance of these parameters on modeled convection and rainfall. Changing the sounding humidity 2%–5% had more impact on rainfall than altering the landscape features. Variability in the West African monsoon may obscure the signal from changes in land cover unless those changes were drastic. Changing individual vegetation characteristics produced small changes in rainfall. Only when the amount of vegetation cover and resistance terms, albedo, and similar parameters were changed together (essentially creating a different land cover) did rainfall patterns shift appreciably. We consider conclusions based on the sensitivity to land cover parameters using a 2D model to be tentative. Given similar initial soil moisture profiles, the results represent lower bounds of the sensitivity of convective lines to land surface conditions in semidesert and broadleaf forest environments. We plan to continue our study of land–atmosphere interaction in West Africa using a more realistic three-dimensional land–atmosphere (cloud resolving) model and consider the synergistic effect of moist (dry) soil and dense (sparse) vegetation.

Acknowledgments. The GCE model is supported by the HQ NASA Physical Climate Program and the TRMM Project. We are grateful to Dr. R. Kakar (HQ NASA) for his support of GCE modeling research and to Pete Wetzel and Barry Lynn for GCE-PLACE coupling. Changhai Liu (NCAR) supplied the sounding used in the simulations. This work benefited from discussions with Aaron Boone, Scott Braun, Greg Jenkins, Chris Lucas, John Molinari, Chris Thorncroft, and Ed Zipser. Helpful suggestions by JHM Editor Ken Mitchell and our anonymous reviewers greatly improved the manuscript. The corresponding author received financial support from NASA Grant NGT 5-81, NSF Grant 0215413, and the University at Albany Professional Development Fund.

REFERENCES

Baker, R. D., B. H. Lynn, A. Boone, W.-K. Tao, and J. Simpson, 2001: The influence of soil moisture, coastline curvature, and

land-breeze circulations on sea-breeze initiated precipitation. *J. Hydrometeor.,* **2,** 193–211.

Betts, A. K., and J. H. Ball, 1995: The FIFE surface diurnal cycle climate. *J. Geophys. Res.*, **100,** 25 679–25 693.

——, and ——, 1998: FIFE surface climate and site-average dataset 1987–89. *J. Atmos. Sci.,* **55,** 1091–1108.

Brubaker, K. L., D. Entekhabi, and P. S. Eagleson, 1993: Estimation of continental precipitation recycling. *J. Climate*, **6,** 1077–1089.

Caniaux, G., J.-L. Redelsperger, and J.-P. Lafore, 1994: A numerical study of the stratiform region of a fast-moving convective line. Part I: General description and water and heat budgets. *J. Atmos. Sci.,* **51,** 2046–2074.

Chalon, J. P., G. Jaubert, F. Roux, and J. P. Lafore, 1988: The West African convective line observed on 23 June during COPT81: Mesoscale structure and transports. *J. Atmos. Sci.,* **45,** 2744–2763.

Chang, C.-Y., and M. Yoshizaki, 1993: Three-dimensional modeling study of convective lines observed in COPT81. *J. Atmos. Sci.*, **50,** 161–183.

Crook, N. A., 1996: Sensitivity of moist convection forced by boundary layer processes to low-level thermodynamic fields. *Mon. Wea. Rev.,* **124,** 1767–1786.

Dudhia, J., M. W. Moncrieff, and D. W. K. So, 1987: The two-dimensional dynamics of West African convective lines. *Quart. J. Roy. Meteor. Soc.*, **113,** 121–146.

Ferrier, B. S., W.-K. Tao, and J. Simpson, 1996: Factors responsible for precipitation efficiencies in midlatitude and tropical convective line simulations. *Mon. Wea. Rev.,* **124,** 2100–2125.

Grabowski, W. W., X. Wu, M. W. Moncrieff, and W. D. Hall, 1998: Cloud-resolving modeling of cloud systems during Phase III of GATE. Part II: Effects of resolution and the third spatial dimension. *J. Atmos. Sci.,* **55,** 3264–3282.

Lafore, J.-P., and M. W. Moncrieff, 1989: A numerical investigation of the organization and interaction of the convective and stratiform regions of tropical convective lines. *J. Atmos. Sci.,* **46,** 521–544.

Lin, Y.-L., R. D. Rarley, and H. D. Orville, 1983: Bulk parameterization of the snow field in a cloud model. *J. Climate Appl. Meteor.,* **22,** 1065–1092.

Liu, C., M. W. Moncrieff, and E. J. Zipser, 1997: Dynamical influence of microphysics in tropical convective lines: A numerical study. *Mon. Wea. Rev.,* **125,** 2193–2210.

Lucas, C., E. J. Zipser, and B. S. Ferrier, 2000: Sensitivity of tropical West Pacific oceanic convective lines to tropospheric wind and moisture profiles. *J. Atmos. Sci.,* **57,** 2351–2373.

Lynn, B. H., W.-K. Tao, and P. J. Wetzel, 1998: A study of landscape generated deep moist convection. *Mon. Wea. Rev.,* **126,** 928–942.

Mohr, K. I., J. S. Famiglietti, A. Boone, and P. J. Starks, 2000: Modeling soil moisture and surface flux variability with an untuned land surface scheme: A case study from the Southern Great Plains 1997 Hydrology Experiment. *J. Hydrometeor.,* **1,** 154–169.

——, ——, and ——, 2001: The effect of sub-grid variability of soil moisture on the simulation of mesoscale watershed hydrology: A case study from the Southern Great Plains 1997 Hydrology Experiment. *Land Surface Hydrology, Meteorology and Climate: Observations and Modeling,* V. Lakshmi, J. Albertson, and J. Schaake, Eds., Amer. Geophys. Union, 161–176.

Nicholls, M. E., R. H. Johnson, and W. R. Cotton, 1988: The sensitivity of two-dimensional simulations of tropical convective lines to environmental profiles. *J. Atmos. Sci.*, **45,** 3625–3649.

Nicholson, S. E., C. J. Tucker, and M. B. Ba, 1998: Desertification, drought, and surface vegetation: An example from the West African Sahel. *Bull. Amer. Meteor. Soc.,* **79,** 815–829.

Prabhakara, C., J. R. Iacovazzi, J. A. Weinman, and G. Dalu, 2000: A TRMM microwave radiometer rain rate estimation method with convective and stratiform discrimination. *J. Meteor. Soc. Japan,* **78,** 241–258.

Roux, F., 1988: The West African convective line observed on 23 June during COPT81: Kinematics and thermodynamics of the convective region. *J. Atmos. Sci.,* **45,** 406–426.

Rutledge, S. A., and P. V. Hobbs, 1984: The mesoscale and microscale structure and organization of clouds and precipitation in midlatitude cyclones. Part XII: A diagnostic modeling study of precipitation development in narrow cold frontal rainbands. *J. Atmos. Sci.*, **41,** 2949–2972.

Tao, W.-K., and J. Simpson, 1993: Goddard Cumulus Ensemble model. Part I: Description. *Terr. Atmos. Oceanic Sci.,* **4,** 35–72.

——, S. Lang, J. Simpson, C.-H. Sui, B. Ferrier, and M.-D. Chou, 1996: Mechanisms of cloud–radiation interaction in the Tropics and midlatitudes. *J. Atmos. Sci.,* **53,** 2624–2651.

——, and Coauthors, 2002: Microphysics, radiation, and surface processes in the Goddard Cumulus Ensemble (GCE) model. *Meteor. Atmos. Phys.,* doi: 10.1007/s00703-001-0594-7.

Weisman, M. L., W. C. Skamarock, and J. B. Klemp, 1997: The resolution dependence of explicitly modeled convective systems. *Mon. Wea. Rev.,* **125,** 527–548.

Wetzel, P. J., and A. Boone, 1995: A Parameterization for Land–Atmosphere–Cloud Exchange (PLACE): Documentation and testing of a detailed process model of the partly cloudy boundary layer over heterogeneous land. *J. Climate*, **8,** 1810–1837.

Xu, K.-M., and D. A. Randall, 1996: Explicit simulation of cumulus ensembles with the GATE Phase III data: Comparison with observations. *J. Atmos. Sci.,* **53,** 3709–3736.